

# High-spectral-resolution fluorescence light detection and ranging for mesospheric sodium temperature measurements

C. Y. She, J. R. Yu, H. Latifi, and R. E. Bills

The principle and practice of narrow-band light detection and ranging (lidar) for temperature measurements are discussed, with emphasis on a new two-frequency technique for measuring mesospheric Na temperature and density profiles. The uniqueness of this narrow-band lidar lies in the transmitter whose line-shape function can be measured directly. The frequency of the laser output can be monitored simultaneously during data acquisition with Doppler-free fluorescence spectroscopy by using a laboratory Na cell. These measurement techniques along with the procedures for data analysis are described in detail. At present the absolute temperature accuracy at the Na layer peak is  $\pm 3$  K ( $\pm 4$  K) with a vertical resolution of 1 km and an integration period of 5 min (2.5 min). Potential applications and further improvements in this lidar technique are also discussed.

*Key words:* Na temperature lidar, mesopause.

## Introduction

Atmospheric temperature, together with its spatial and temporal variations, is the fundamental parameter that needs to be determined accurately in studies of atmospheric chemistry and dynamics. No known technique can be used to measure the temperature through all atmospheric regions. In the upper stratosphere the mesosphere and lower thermosphere regions, which are too high for aircraft or a balloon technique and too low for orbiting satellite measurement, are difficult to study experimentally. Rocket launched falling spheres,<sup>1</sup> grenades,<sup>2</sup> airglow observations,<sup>3</sup> and nadir viewing satellites<sup>4</sup> such as Nimbus 6 and 7 have all provided useful information on the temperature of the mesopause region. However, none of these techniques is capable of providing the temporal resolution and long-term coverage needed for detailed studies of small-scale temperature variations.

Light detection and ranging (lidar) is one of the remote-sensing techniques that offer the greatest promise for high-resolution observations of the temperature structure of the atmosphere. Existing lidar techniques for temperature measurements that could be used routinely rely on broadband Rayleigh scattering from which vertical air density distribution is measured. By assuming hydrostatic and local thermodynamic equilibrium, atmospheric temperature profiles can be calculated from the molecular backscatter profile. Stratospheric and mesospheric temperature profiles can indeed be obtained this way, although its accuracy at upper altitudes is impeded somewhat by the lack of an accurate end-point value in temperature and by the presence of stratospheric aerosol layers. Broadband Rayleigh lidars are now used routinely to measure temperature profiles from  $\sim 30$ - to 80-km altitude.<sup>5</sup> Air density, however, cannot be determined by broadband molecular (Rayleigh) scattering with any accuracy in both the troposphere/lower stratosphere (below 30 km) and the upper mesosphere (above 80 km) because of, respectively, the interference of aerosol and the small signal resulting from increased distance and reduced molecular density.<sup>6</sup> For tropospheric measurements Shimizu *et al.*<sup>7</sup> have proposed the use of a narrow-band lidar together with an atomic vapor blocking filter to permit molecular scattering to be detected and temperature determined by completely rejecting the aerosol-scattering contribution. The details of this tropo-

---

When this research was done C. Y. She and H. Latifi were with the Department of Physics, Colorado State University, Fort Collins, Colorado 80523. J. R. Yu is with the Electrical Engineering Department, Colorado State University, Fort Collins, Colorado 80523. R. E. Bills is with the Department of Electrical and Computer Engineering, University of Illinois, Urbana-Champaign, Illinois 61810. H. Latifi is now with the University of Shahid Beheshti, Tehran, Iran.

Received 12 October 1990.

0003-6935/92/122095-12\$05.00/0.

© 1992 Optical Society of America.

spheric measurement technique are not discussed here. Theoretically one can extend the broadband Rayleigh technique to measure temperatures at altitudes that exceed even 100 km. However, to study gravity wave perturbations at mesopause heights, signal levels of the order of  $10^4$ – $10^5$  counts are required.<sup>8</sup> To measure atmospheric temperature profiles with high accuracy and resolution at this signal level, a more efficient method is needed. Since the Na fluorescence cross section is more than 14 orders higher than the Rayleigh-scattering cross section<sup>6</sup> at 589 nm, depending on air density and the natural Na abundance near the mesopause,<sup>9</sup> the signal level of a Na fluorescence lidar is typically  $2 \times 10^4$  times stronger than that of a Rayleigh-scattering lidar with the same laser power and receiving telescope aperture. The structure of the Na  $D_2$  electric-dipole transition has been determined to fractions of megahertz accuracy.<sup>10</sup> The Na  $D_2$  fluorescence spectrum consists of two groups of lines,  $D_{2a}$  and  $D_{2b}$ , which are formed by the hyperfine levels of the Na ground state. It shows two distinct Doppler-broadened peaks separated by  $\sim 1.772$  GHz. Since the Na atoms are in local thermal equilibrium with air molecules and the Doppler-broadened fluorescence spectrum is temperature dependent, the mesopause temperature can therefore be determined with great accuracy and resolution by a narrow-band Na fluorescence lidar.

This idea was first applied by Gibson *et al.*<sup>11</sup> who were able to deduce the temperature near the peak of the Na layer. More recently Fricke and von Zahn<sup>12</sup> obtained Na temperature profiles with 1-km resolution and 10 K accuracy by using an excimer-pumped dye-laser system. They pointed out that the ratio of the fluorescence signal at the stronger  $D_{2a}$  peak to that at the minimum between the two peaks is an extremely sensitive indicator of temperature. However, since the frequency of a pulsed laser is neither reproducible nor predictable, they had to measure the frequency of each individual laser pulse and interrogate a wide-frequency scan to cover enough of the relevant spectrum. Although the full wave at half-maximum (FWHM) can be estimated, the detailed line shape of their laser cannot be determined, which limits efficiency and accuracy. The Bonn group demonstrated the capabilities of routine Na temperature measurements and have published several excellent lidar studies of the mesopause temperature structure above Andoya, Norway.<sup>13,14</sup>

To determine the mesospheric temperature from the ratio of fluorescence signals at two frequencies, the laser line shape and the absolute frequency of the tunable laser must be known and should remain constant from pulse to pulse. To accomplish this She *et al.*<sup>15</sup> recently used a laser system that is based on a stabilized cw single-mode tunable dye laser and followed it by a pulsed dye amplifier. The pulsed dye amplifier is pumped by a doubled yttrium aluminum garnet (YAG) laser. Temperature measurements near the Na layer peak of  $\pm 3$  K and a vertical resolution of 1 km have been demonstrated with an integration

period of 5 min. We discuss the physics background of the Na temperature measurement based on the narrow-band fluorescence lidar and in particular the details of the two-frequency Na temperature lidar. The measurement of the laser line shape, the use of Doppler-free fluorescence spectroscopy for absolute frequency monitoring, the procedures for data analysis, and the factors that affect the accuracy of mesospheric temperature measurements are discussed.

### Na Fluorescence Spectra and Temperature Determination

The energy levels of both the ground state ( $3s \ ^2S_{1/2}$ ) and the excited state ( $2p \ ^2P_{3/2}$ ) of the Na  $D_2$  transition are shown in Fig. 1(a). The hyperfine splittings of the excited state were experimentally determined to within  $\pm 0.4$  MHz,<sup>10</sup> while the splitting of the ground state was first determined to be<sup>16</sup> 1771.62615(25) MHz and then more recently to be<sup>17</sup> 1771.626129(2) MHz. Doppler-broadened fluorescence spectra at several atmospheric temperatures of the transition are shown in Fig. 1(b). The characteristic double peaks are the result of the hyperfine splitting in the Na ground state, while the width of the individual peaks is the result of thermal Doppler broadening. Since the

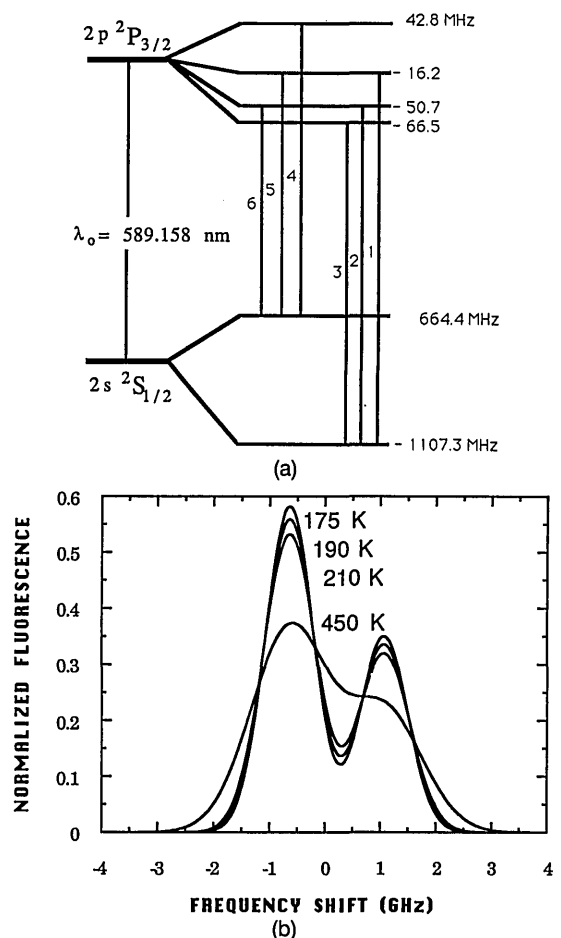


Fig. 1. (a) Energy levels and (b) Doppler-broadened fluorescence spectra of Na  $D_2$  transitions. The six electric-dipole allowed hyperfine transitions are labeled in descending order of transition frequencies as described in Table I.

energy levels of the Na atom are known to a high degree of accuracy and at the mesopause the collisional broadening is negligible, the shape function of the Doppler-broadened Na D<sub>2</sub> fluorescence spectrum depends only on temperature. The mathematical function is precisely known and is given as

$$g(\nu) = (D/\pi T)^{1/2} \sum_{n=1}^6 A_n \exp[-D(\nu - \nu_n)^2/T], \quad (1)$$

where  $D = m\lambda_0/2k_B = 497.6165 \text{ K (ns)}^2$ . The parameters  $m$ ,  $\lambda_0 = 589.158 \text{ nm}$ ,  $k_B$ ,  $A_n$ , and  $\nu_n$  are, respectively, the mass of the Na atom, the mean Na D<sub>2</sub> transition wavelength, the Boltzmann constant, and the relative line strengths (or transition probability) and frequencies of the six electric-dipole-allowed D<sub>2</sub> transitions. Table I gives numerical information<sup>10,12</sup> about these transitions. Here the weighted center of the six transitions, weighted by  $A_n$ , is used as the zero-frequency reference. It is apparent from Fig. 1(b) and Eq. (1) that the local temperature may be determined either by fitting the measured fluorescence signal over a selected range of frequencies to the temperature-dependent theoretical function, i.e., the scanning method as carried out by Fricke and von Zahn,<sup>12</sup> or by comparing the measured ratio of fluorescence intensities at two properly chosen frequencies with the calculated temperature-dependent intensity ratio, i.e., the two-frequency method as carried out by She *et al.*<sup>15</sup> Everything else being equal the temperature accuracy that is obtained with either the scanning method or the two-frequency method should be comparable. Since at a given temperature the spectrum of the laser-induced fluorescence is the convolution of the laser line shape with the thermal Doppler-broadened Na D<sub>2</sub> fluorescence spectrum, as shown in Fig. 1(b), one must then use a narrow-band laser system with a measurable line-shape function to retrieve experimentally the spectral, thereby temperature-dependent, information from the induced fluorescence of atmospheric Na atoms. Since the strength of the detected fluorescence signal depends on the excitation frequency, the success of either method depends on having a stable, tunable, and narrow-band laser transmitter whose center frequency as well as line shape can be characterized accurately against a known absolute frequency scale. Such a frequency marker should be conveniently available

during the data acquisition phase of the lidar operation.

To determine the frequency of the laser output to an accuracy of a few megahertz we use a laboratory Na vapor cell for the two-frequency method. The Na cell is heated to  $\sim 325 \text{ K}$  so that its fluorescence induced by the cw laser can be monitored easily with a photomultiplier operated in the current mode. The fluorescence spectrum is not a sensitive function of the cell temperature. The Doppler-broadened width at 325 K, which is calculated to be 1.36 GHz FWHM, is too broad to be useful as an accurate frequency reference to set the frequency of the lidar transmitter. Fortunately the rear window of the vapor cell reflects laser light in the backward direction. Under the simultaneous illumination of two counterpropagating beams at a saturated laser intensity the Na fluorescence spectrum shows Doppler-free features at D<sub>2a</sub> and D<sub>2b</sub> peaks as well as at the crossover resonance. These features are similar to those observed with the well-known Doppler-free saturated absorption spectroscopy.<sup>18</sup> The resulting fluorescence spectrum is shown in Fig. 2(a). In addition to the highly distorted Doppler profile the three Doppler-free features are clearly seen. To make sure that these Doppler-free fluorescence features are indeed the result of simultaneous illumination of two counterpropagating beams, we repeated the experiment and purposely enhanced the reflected beam by using a mirror to send the laser beam back into the cell. The result is shown in Fig. 2(b). Notice that the Doppler-free features, especially at the D<sub>2a</sub> and crossover frequencies, are much enhanced. Using these Doppler-free features as the frequency markers, we show the result of a mesopause Na fluorescence scan that is taken with our lidar system as data points in Fig. 2(b). Each data point represents the fluorescence of the Na layer at  $92 \pm 0.5 \text{ km}$  averaged over 1200 laser shots, normalized by Rayleigh scattering, and corrected for Na absorption. This scan is seen to be consistent with a theoretically calculated Doppler-broadened spectrum at a temperature of 187 K [shown by the dashed curve in Fig. 2(b)].

In previous papers<sup>15,19</sup> we stated that because of the theoretical and experimental uncertainties we can only assign the location of these features to within  $\pm 10 \text{ MHz}$ , respectively, at  $\nu_a = -648.8 \text{ MHz}$ ,  $\nu_b = 1066.9 \text{ MHz}$ , and  $\nu_c = 200.3 \text{ MHz}$ . In an attempt to

Table I. Parameters and the COM's of the Na D<sub>2</sub> Hyperfine Transitions<sup>a</sup>

Group	Transition $n$	$^2S_{1/2}$	$^2P_{3/2}$	Offset (GHz) $\nu_n$	COM (GHz)	Relative Line Strength $A_n$
D <sub>2b</sub>	1	$F = 1$	$F = 2$	1.0911	1.0683	5/32
	2		1	1.0566		5/32
	3		0	1.0408		2/32
D <sub>2a</sub>	4	$F = 2$	$F = 3$	-0.6216	-0.6410	14/32
	5		2	-0.6806		5/32
	6		1	-0.7150		1/32

<sup>a</sup> $F$  is a quantum number of the energy level that denotes the angular momentum of the atom. COM is the center of mass of the transition group.

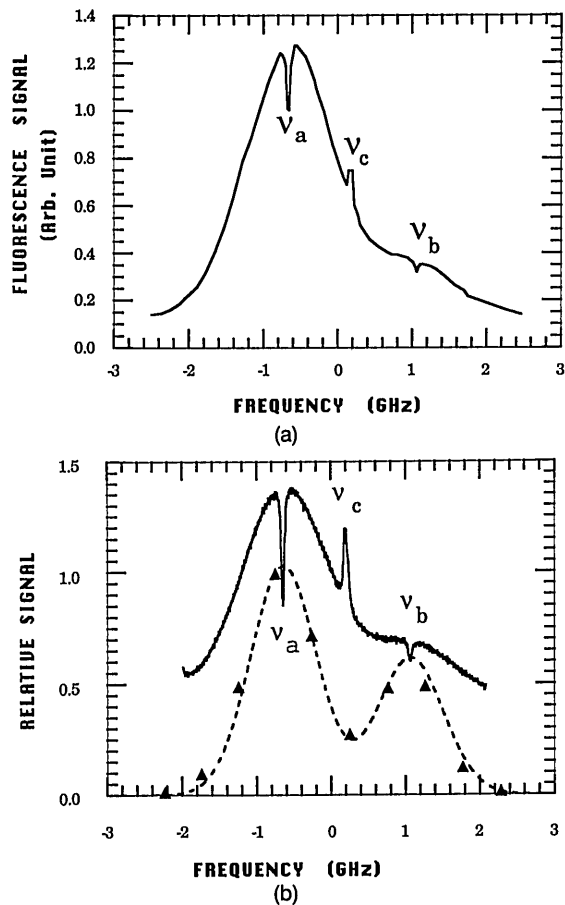


Fig. 2. Saturated Na  $D_2$  fluorescence spectra (a) with the reflection from the window of the Na cell and (b) with enhanced reflection from a mirror. Three dominant Doppler-free features are seen clearly. They are located at  $\nu_a$  near the  $D_{2a}$  peak,  $\nu_b$  near the  $D_{2b}$  peak, and  $\nu_c$  at the crossover resonance that is between. Shown also in (b) is the fluorescence signal from a mesospheric Na layer at 92 km and the theoretical Doppler-broadened spectrum for  $T = 187$  K (shown by the dashed curve).

shed light on the logic behind these frequency assignments, we discuss briefly the absorption (and fluorescence) spectroscopy of Na  $D_2$  transitions. Since the triplets in either the  $D_{2a}$  or  $D_{2b}$  transitions cannot be resolved completely, they may be considered as overlapped absorption lines with their peaks located at their centers of mass (COM's), respectively, at  $-0.6410$  and  $1.0683$  GHz as listed in Table I. COM is calculated by using line strengths as the weighting factors.

Under the simultaneous illumination of the counterpropagating narrow-band laser beams, atoms experience velocity-dependent absorption (thus Doppler-free fluorescence). At each allowed transition atoms at rest can absorb photons from both laser beams, which leads to saturated absorption at these frequencies. This is not the case for moving atoms. In addition for each pair of allowed transitions at the frequencies  $\nu_i$  and  $\nu_j$  from a ground level there exists a crossover resonance at their mean frequency  $(1/2)(\nu_i + \nu_j)$ . For  $D_{2a}$  or  $D_{2b}$  transitions these crossover

resonances with a common lower level, as depicted in Fig. 3(a), are due to saturated absorption of atoms whose longitudinal motion gives a Doppler shift of  $(1/2)|\nu_i - \nu_j|$ . Since there are three allowed transitions in each  $D_2$  transition group, there should be three crossover resonances in each group. Including those crossover resonances with the weighting factors given in Table II, the COM's for the  $D_{2a}$  and  $D_{2b}$  Doppler-free transition frequencies are calculated to be  $-0.6567$  and  $1.0656$  GHz, respectively. Since the exact line shape of these features is strictly speaking intensity dependent, we used the average of these values and the values in Table I, where the contribution of the crossover resonances is ignored and set the COM's at  $\nu_a = -648.8$  MHz and  $\nu_b = 1066.9$  MHz in the previous papers.<sup>15,19</sup>

Because the ground levels of the  $D_{2a}$  and  $D_{2b}$  transitions are separated by  $1.772$  GHz, an atom moving along the beams with a speed corresponding to a Doppler shift of  $886$  MHz can interact resonantly with both counterpropagating beams, if the transitions from both ground levels to a common upper level are allowed. One beam could excite such an atom from one ground level, while the other beam could then deexcite it to the other ground level. In this manner the counterpropagating beams together recycle the atom between its two ground levels. As a result all atoms in this speed group can absorb photons from both beams, thereby increasing the probability of their excitation. An atom with a Doppler shift other than  $886$  MHz can absorb photons only from one of the two beams depending on its direction of motion. For this Doppler-free transition with a common upper level to occur, as depicted schematically in Fig. 3(b), the laser frequency should be  $(1/2)(\nu_i + \nu_j) = \nu_j - 886 = \nu_i + 886$  MHz, where  $\nu_i$  and  $\nu_j$  are the allowed transition frequencies from different ground levels. There are two such crossover resonances resulting from the pairs of transitions indicated in Table II as 5-1 and 6-2. The third relevant type of crossover resonance, which consists of two upper levels (separated in frequency by  $\Delta$ ) and two lower levels, is

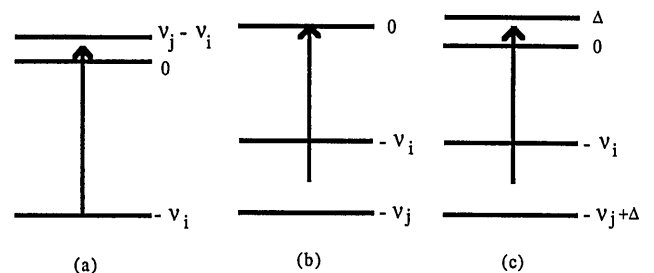


Fig. 3. Schematic energy diagrams for crossover resonances (a) with a common lower level, (b) with a common upper level, and (c) with two lower and two upper levels. In (c) transitions from at least one upper level to both lower levels must be allowed. The arrows indicate the crossover resonance at the mean frequency of the two allowed transitions,  $\nu_i$  and  $\nu_j$ . At mesopause temperatures only the common lower level in (a) is populated, while both lower levels in (b) and (c) are populated.

**Table II. Parameters and the COM of the Doppler-free Na D<sub>2</sub> Hyperfine Transitions Including Crossover Resonances**

Group	Transition	Offset (GHz)	COM (GHz) <sup>a</sup>	Relative Line Strength
D <sub>2b</sub>	1	1.0911	ν <sub>a</sub> = 1.0656	5/36
	1-2	1.0738		10/36
	1-3	1.0660		7/36
	2	1.0566		5/36
	2-3	1.0487		7/36
	3	1.0408		2/36
Crossover	4-5-1	0.2347	ν <sub>c</sub> = 0.2039	24/94
	4-6-2	0.2175		20/94
	5-1	0.2053		10/94
	5-6-1-2	0.1880		16/94
	5-1-3	0.1801		10/94
	6-2	0.1708		6/94
	6-2-3	0.1629		8/94
D <sub>2a</sub>	4	-0.6216	ν <sub>b</sub> = -0.6567	14/60
	4-5	-0.6507		19/60
	4-6	-0.6683		15/60
	5	-0.6806		5/60
	5-6	-0.6978		6/60
	6	-0.7150		1/60

<sup>a</sup>COM is the center of mass of the transition group.

schematically depicted in Fig. 3(c). Although there are two upper levels, at least one must be transitionally connected to both ground levels for the crossover resonance to occur. There are five distinct crossover resonances of this type involving transitions 4-5-1, 4-6-2, 5-6-1-2, 5-1-3, and 6-2-3 as listed in Table II. These resonances occur at the laser frequency of  $(\frac{1}{2})(\nu_i + \nu_j) = \nu_j - (886 + \Delta/2) = \nu_i + (886 + \Delta/2)$  MHz, while the atoms taking part in resonance are moving with a Doppler shift of  $(886 + \Delta/2)$ . If each upper level is connected to a separate lower level, as in the case of the transition pair 3-4, the counterpropagating beams cannot mix the two ground levels of the atom and there will be no crossover resonance of this type. Although a detailed study is necessary we assume for simplicity that the relative strength of the crossover transition at the respective mean frequency is proportional to the sum of the line strengths of the associated transitions. Using the weighting factors so stated, we calculate the value of ν<sub>c</sub> to be ν<sub>c</sub> = 203.9 MHz; this is close to the previously used value of 200.3 MHz. Since the crossover resonances of all three types exist at all intensity levels, we now suggest the use of the COM's calculated with the inclusion of all crossover resonance contributions given in Table II and assign the frequencies of the three Doppler-free features as ν<sub>a</sub> = -656.7 MHz, ν<sub>b</sub> = 1065.6 MHz, and ν<sub>c</sub> = 203.9 MHz. Although the energy levels of the Na D<sub>2</sub> transitions are known to ±0.4 MHz,<sup>10</sup> the position of the Doppler-free features cannot be located experimentally to the same accuracy because of the natural and power-broadened linewidth of each component as well as the frequency jitters that exist in the ring dye laser. Because of these

experimental uncertainties, the error bar in ν<sub>a</sub>, ν<sub>b</sub>, and ν<sub>c</sub> remains at ±10 MHz. The experimental uncertainty can be improved only after careful study of the structure of the Doppler-free features. A more detailed study of the saturated Na fluorescence spectroscopy is under way.

### Narrow-Band Lidar and Characterization of Its Transmitter

A block diagram of the narrow-band lidar transmitter that satisfies the requirements mentioned above is shown in Fig. 4. Such a lidar instrument has been used for the two-frequency mesospheric Na temperature measurements at Fort Collins, Colo.<sup>15</sup> The laser beam starts from a tunable cw single-mode dye laser that is pumped by a cw Ar-ion laser. Its output is amplified by a pulsed dye amplifier, which is pumped by an injection-seeded doubled YAG laser at a pulse rate of 20 Hz. The output of this system consists of a tunable, megawatt, narrow-band beam of pulses with a measured FWHM of ~4.2 ns. The typical energy per pulse has been measured to be 30 mJ with 0.2% or less of amplified spontaneous emission. To determine the characteristics of this laser system, several monitoring devices are used. The center frequency is set by tuning the cw single-mode dye laser, first monitored with a wavelength meter for a general wavelength selection and then with Doppler-free fluorescence spectroscopy for accuracy. The wavelength meter searches for the Na D<sub>2</sub> line. The saturated Doppler-free fluorescence spectroscopy technique, which is referenced to a vapor cell, can be used to set the absolute frequency of the cw single-mode dye laser to within ±10 MHz. To determine the laser line-shape function of the pulsed output a small portion of the output is sent through a Fabry-Perot étalon to measure the line shape. As the laser frequency is scanned the transmission function of the pulsed output through this étalon is recorded simultaneously with the transmission function of the cw laser through a longer confocal Fabry-Perot interfer-

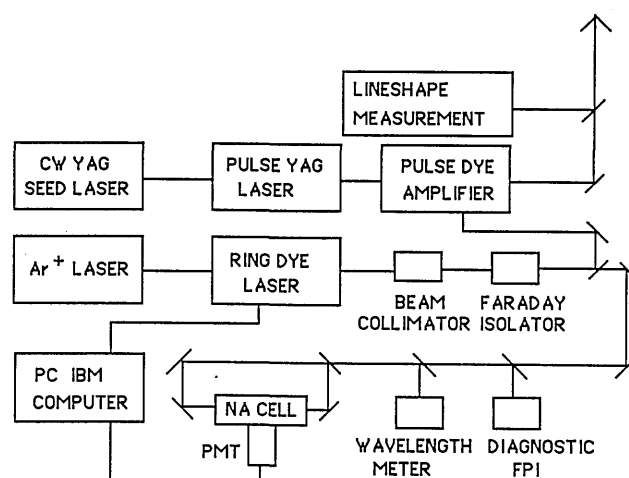


Fig. 4. Na temperature lidar transmitter block diagram.

ometer that has a free spectral range of 75 MHz. The second transmission function is then used as the frequency marker with which the line-shape function, i.e., the first transmission function, of the pulsed output is compared.

By using a 500-MHz real-time oscilloscope the intensity of the pulsed output  $I(t)$  can be measured with a fast diode. An example is shown in Fig. 5(a). The measured rms intensity width for this example is  $\Delta t = 1.93$  ns. Although the intensity profile is not symmetric, it is seen to be quite smooth because the amplifier is pumped by an injection-seeded Nd:YAG laser. If no phase modulation exists in the laser beam the pulsed output is said to be Fourier transform limited. In this case the amplitude of its normalized electric field  $h(t)$  is proportional to  $[I(t)]^{1/2}$ . The transform-limited power spectral density  $S_0(\nu)$  of the pulse is the absolute square of the Fourier transform of  $h(t)$ :

$$H(\nu) = \int h(t) \exp(i2\pi\nu t) dt. \quad (2)$$

The transform-limited power spectral density  $S_0(\nu) = |H(\nu)|^2$  for the intensity profile given in Fig. 5(a) has been evaluated numerically, and its result is given in Fig. 5(b). The rms spectral width of  $S_0(\nu)$  is measured to be  $\Delta\nu = 0.0514$  GHz, which gives rise to a

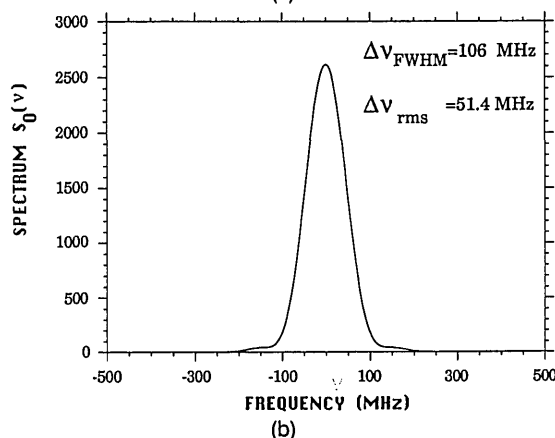
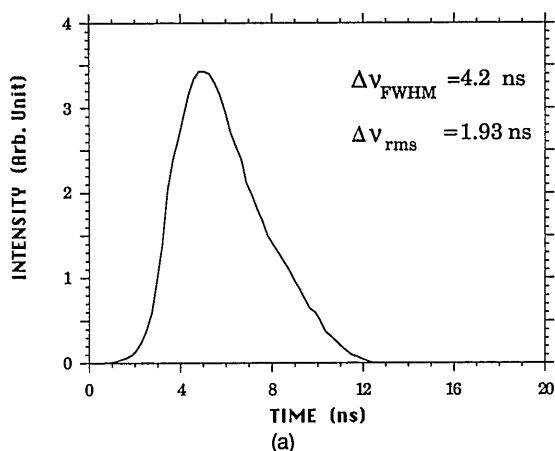


Fig. 5. Intensity profile of (a) the pulsed output and (b) its transform-limited spectrum (b).

transform-limited product of  $\Delta t \Delta\nu = 0.10$ . This value should be compared with the minimum uncertainty product of the transform-limited Gaussian pulse,  $\Delta t \Delta\nu = 1/4\pi = 0.08$ . Since the actual pulsed output may not be precisely Fourier transform limited, we measure its power spectral density  $S(\nu)$  directly by using the procedure outlined previously. The result of a sequence of five power spectral density functions, two of which are shown in Fig. 6, yields a rms width of  $\Delta\nu = 63.49 \pm 1.06$  MHz. Thus the measured uncertainty product is  $\Delta t \Delta\nu = 0.12$ , which is larger than the transform-limited value of 0.10, which suggests the fact that the laser beam has picked up some phase modulation (or frequency chirp) as it passed through the amplifier. A representative line-shape function with a rms width of  $\Delta\nu_{\text{rms}} = 0.0643$  GHz is shown as the curve marked measured and is compared with two hypothetical line shapes with Gaussian and Lorentzian functions in Fig. 7(a). All three line-shape functions have the same FWHM of 112 MHz but different rms widths.

The spectrum of laser-induced fluorescence, which depends on the laser line-shape function  $S(\nu)$ , is the convolution of the normalized line-shape function and the thermal Doppler-broadened spectrum  $g(\nu)$ . The measured intensity ratio at the two selected frequencies (the intensity at  $\nu_c$  to that at  $\nu_a$ )  $R$  is a unique function of the Na temperature for a given laser line-shape function. Using the measured line-shape function of Fig. 7(a), we can evaluate the conversion (calibration curve) between the intensity ratio  $R$  and the Na temperature  $T$ ; it is shown as the line marked measured in Fig. 7(b). We point out that the calibration curve depends not only on the FWHM linewidth of the laser but also on the laser line-shape function. This is evident when calibration curves of the three line-shape functions of Fig. 7(a) along with a line corresponding to an ideal laser (with a delta function as its spectrum) are compared in Fig. 7(b). It is seen that differences in the line shape may result in a temperature uncertainty as large as 20 K. The ratios in Fig. 7(b) were calculated at the new frequencies  $\nu_a = -656.7$  MHz and  $\nu_c = 203.9$  MHz. If the

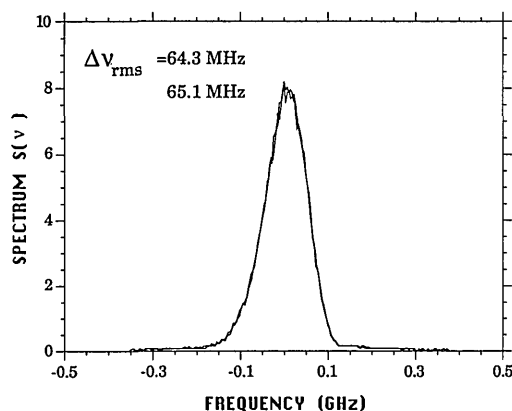
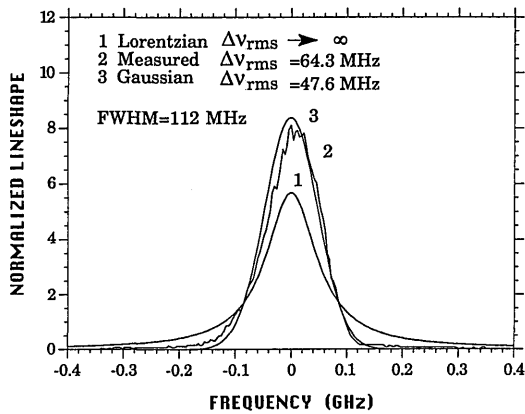
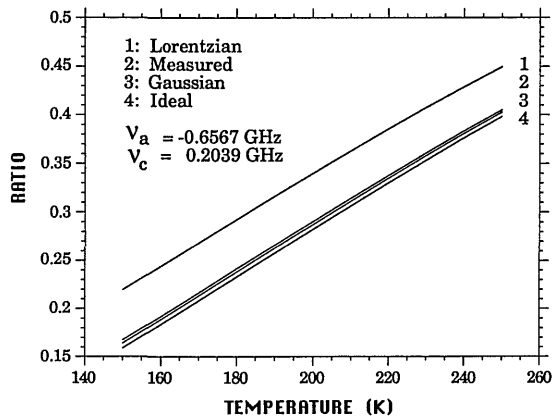


Fig. 6. Two measured laser spectra (power spectral density functions)  $S(\nu)$  after amplifier alignment.



(a)



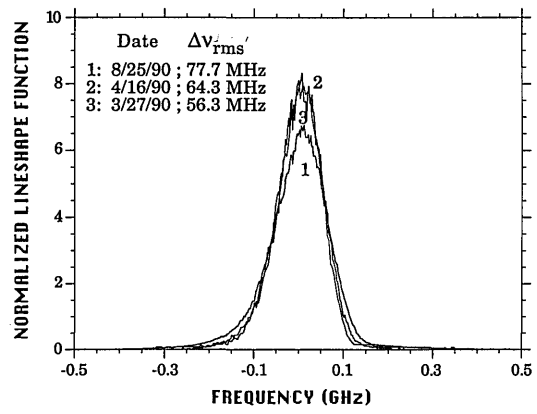
(b)

Fig. 7. (a) Three laser line-shape functions: a measured line shape, 2, along with two hypothetical line shapes, 1 and 3, with equal FWHM = 112 MHz. (b) The temperature calibration lines of these line shapes compared with that of an ideal laser.

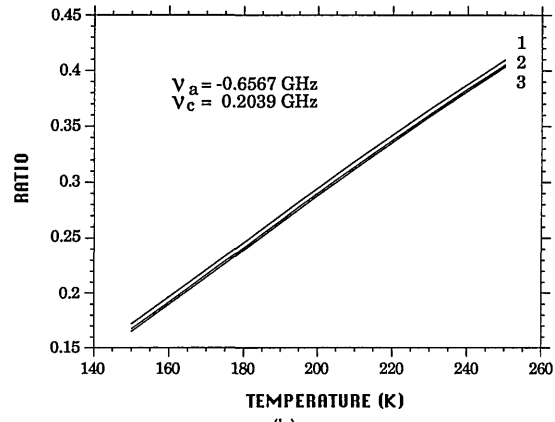
previous values of  $\nu_a = -648.8$  MHz and  $\nu_c = 200.3$  MHz were used, the temperature would be lower by  $< 2$  K for the same intensity ratio.

It should be pointed out that the line-shape function of the pulsed laser output depends on the amplifier alignment. It therefore should be measured for the calculation of the calibration curve whenever a realignment of the laser amplifier is made. Up to this point we have checked the line-shape functions after four different alignments. The laser line-shape functions are found to be reproducible within 1 MHz for a given amplifier alignment. As given previously the five measurements of the laser line shapes on 16 Apr. 1990 gave a rms width of  $\Delta\nu_{\text{rms}} = 63.49 \pm 1.06$  MHz. Similar five measurements on 25 Aug. 1989 gave  $\Delta\nu_{\text{rms}} = 77.68 \pm 0.21$  MHz, which indicate the variability between alignments. Three representative line-shape functions, one for each laser amplifier alignment, are shown in Fig. 8(a). Their corresponding calibration lines are shown in Fig. 8(b); they show a range of  $< 4$  K. Because the laser line-shape function is often asymmetric, its rms width  $\Delta\nu_{\text{rms}}$  appears to be a better figure of merit for line-shape characterization.

A Fresnel lens with a 1.22-m diameter is used to



(a)



(b)

Fig. 8. Representative measured line-shape functions (a) and their associated temperature calibration lines (b), each corresponding to a different laser amplifier alignment.

collect fluorescence photons into a photomultiplier with a red-sensitive GaAs cathode surface. The characteristics of the lidar are summarized in Table III. If a reflecting mirror of the same diameter becomes available, the level of the received signal is increased considerably because a Fresnel lens has a relatively high scattering loss.

#### Procedure for Two-Frequency Mesospheric Temperature Measurement

Since the frequency of the crossover resonance at  $\nu_c = 203.9$  MHz is extremely close to the minimum between the two Doppler-broadened peaks (at 300 MHz for 200 K), we take advantage of the ease in tuning the laser to the Doppler-free features of the reference fluorescence spectrum and choose  $\nu_a$  and  $\nu_c$  as the two operational frequencies for the mesospheric temperature measurements. An added advantage of this choice lies in the fact that unlike the frequencies at the  $D_{2a}$  peak and the minimum between the two Doppler-broadened peaks,  $\nu_a$  and  $\nu_c$  are temperature independent. For data acquisition we tune the laser frequency to  $\nu_a$  and then to  $\nu_c$  and fire 1200 (or 600) laser shots at each frequency. The time for tuning the laser to obtain both photon-count profiles (at  $\nu_a$  or  $\nu_c$ ) takes  $\sim 2$  (or 1) min. Selection of the photon-counting

Table III. Characteristics of the Na Temperature Lidar

Transmitting System		Receiving System	
Wavelength	589 nm	Telescope 1.22-m-diameter Fresnel lens	
Pulse energy	30 mJ (typical)	Aperture area	1.17 m <sup>2</sup>
Pulse rate	20 pps	Field of view	3 mrad
Average power	600 mW	Optical bandwidth	20 Å FWHM
Beam divergence	1 mrad FW	Range resolution	37.5 (75) m
Polarization	45° ± 5° Linear to magnetic north		

electronics permits photon-count profiles with a 37.5-m (or 75-m) range length to be taken throughout the night, weather permitting. When the range-resolved profiles of the fluorescence photon counts at  $\nu_a$  and  $\nu_c$  are properly analyzed, the temporal evolution of Na temperature and density distribution may be displayed.

To ensure the correct operation of the Na temperature lidar, not only the Doppler-free saturated fluorescence of the vapor cell is used to guide the laser tuning, it is also used to monitor simultaneously the frequency of the laser at  $\nu_a$  or  $\nu_c$  during data acquisition. Since the features at these frequencies are extremely sharp as shown in Fig. 2(b), a frequency within  $\pm 10$  MHz can be monitored easily. For the determination of the calibration curve the laser line-shape functions are measured at the beginning and the end of data acquisition by the procedure that was outlined previously. As pointed out previously the measured line-shape functions between major amplifier realignment procedures are quite repeatable. If the Na  $D_2$  fluorescence spectrum is taken with a higher spectral resolution, the structures of the  $D_{2a}$  peak as well as the crossover resonance can be resolved better as shown in Fig. 9. The frequency scale was determined from the frequency marker that was provided by the longer confocal diagnostic Fabry-Perot interferometer (free spectral range  $\sim 75$  MHz) with the zero-frequency reference shifted to a chosen location. If the two frequencies for Na lidar operation were chosen from selected features in the fine struc-

tures of the  $D_{2a}$  peak and the crossover resonance, as shown in the insets of Fig. 9, a laser-frequency error of less than  $\pm 10$  MHz could be achieved. In this case a higher accuracy in temperature measurements than presently claimed is possible.

### Experimental Results and Data Analysis

Using the above narrow-band lidar transmitter and experimental procedure, we made the initial two-frequency mesospheric temperature measurements during the nights of 22–24 August 1989 at Fort Collins, Colo. (41.6° N, 105° W). The preliminary results and interpretation of these measurements have been published.<sup>15</sup> The data from August 1989 were collected by tuning the laser to the  $D_{2a}$  peak, accumulating the photon returns from 1200 laser shots, and then tuning to the crossover resonance and accumulating another 1200 shots. The advanced lidar data-acquisition system<sup>20</sup> with a range length of 37.5 m was used for data acquisition. The laser was tuned manually by adjusting the voltage of the transducer that controlled the effective cavity length of the ring laser. Approximately 1 min was required for tuning from one frequency to the other. The frequency of the cw dye laser was continuously monitored by the saturated fluorescence signal of the Na vapor cell.

There are several sources of potential temperature errors including saturation effects<sup>21,22</sup> caused by high laser intensity and the Hanle effect,<sup>12</sup> which has to do with the dependence of the relative hyperfine line strengths on the orientation of the laser polarization with respect to the Earth's magnetic field. Saturation effects were studied first and quantified for broad-band pulsed lasers by Megie *et al.*<sup>21</sup> Since for the same pulse energy, pulse width, and beam divergence, the saturation effects can be much more severe for a narrow-band laser, Welsh and Gardner<sup>22</sup> have considered the saturation effects on a pulse laser with a bandwidth of 0.13, which is comparable to our laser linewidth. They concluded that the minimum beam divergence allowed that ensures negligible saturation effects for such a laser with 30-mJ pulse energy and 2-ns rms width is  $\sim 0.65$  mrad. The beam divergence of our laser output has been measured to be 1.0 mrad, which suggests that the measured temperature caused by saturation effects may be  $\sim 1$  K higher. Fricke and von Zahn<sup>12</sup> have analyzed the Hanle effect at Bonn, and they found that the measured temperature difference between east-west and south-north linearly polarized lidars is  $\sim 4$  K. Since our laser beam was linearly polarized at  $45^\circ \pm 5^\circ$  to the magnetic north,

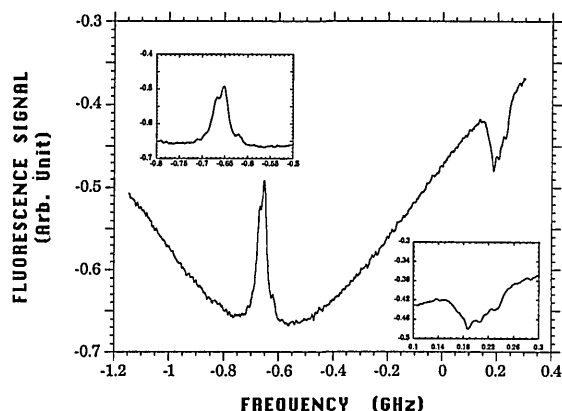


Fig. 9. Structure of the  $D_{2a}$  peak and crossover resonance with higher spectral resolution. The frequency scale was determined from the frequency marker provided by the diagnostic Fabry-Perot interferometer (free spectral range  $\sim 75$  MHz) with the zero-frequency reference shifted to a chosen location.

our use of the spatially averaged line strengths for calculating the calibration curves introduces a negligible additional error to the presently claimed accuracy. Other error sources and their effects on temperature uncertainty for this set of experiments are summarized in Table IV. The details of these sources and their error assessment have been discussed elsewhere<sup>15,19</sup> and are not repeated here. Since the method for determining temperature from the measured intensity ratio assumes a constant Na density during the experiment, density variations between the  $D_{2a}$  and crossover profiles should be minimized. For this reason four (three) consecutive photon-count profiles obtained with a laser tuned to  $\nu_a$  ( $\nu_c$ ) were then added by using the weighting factors of 1/15, 1, 1, 1/15 (3/10, 1, 3/10) to form a pair of crossover and  $D_{2a}$  peak files, which gives rise to an equivalent data integration period of 5 min. The weighting factors were suggested by She *et al.*<sup>15</sup> and so chosen that only the sixth and higher-order temporal variations of density influences the final temperature profiles. Even with this procedure it can be seen from Table IV that Na and atmospheric density variations still compete with photon noise for the dominant error source for Na temperature measurements. Thus an absolute temperature accuracy at the Na layer peak of  $\pm 3$  K with a vertical resolution of 1 km and an integration period of 5 min was achieved in this set of experiments.

With minor modifications the narrow-band Na temperature lidar was operated at Fort Collins, Colo., again during March and April 1990 in support of the ALOHA '90 airborne campaign.<sup>23</sup> To reduce the temporal density variations further, these data were collected by tuning the laser to the  $D_{2a}$  peak while accumulating the photon returns from 600 laser shots and then tuning to the crossover resonance while accumulating another 600 shots. This process was repeated continuously throughout the observation period. A commercial data-acquisition system electronics with a range length resolution of 75 m were used for data acquisition. The laser was tuned semiautomatically by a computer that required  $< 0.5$  min for tuning from one frequency to the other. This

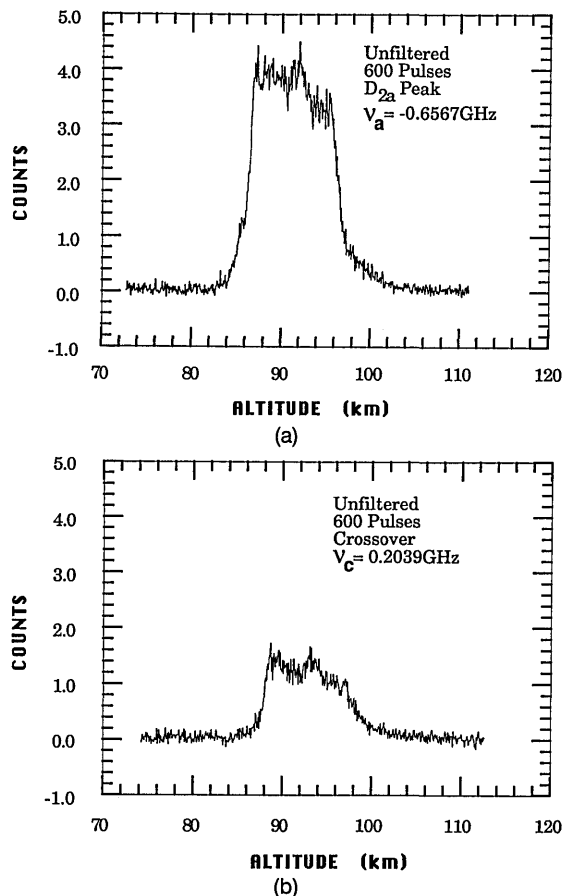


Fig. 10. Mesospheric Na fluorescence excited by the laser at (a) the  $D_{2a}$  peak and (b) the crossover resonance after background subtraction and intensity normalization with Rayleigh scattering.

tuning time can be reduced further in the future. Although the data that were obtained during the campaign have not yet been analyzed fully, a set of 16 photon-count profiles (eight at  $\nu_a$  and eight at  $\nu_c$ ) taken on 2 March 1990 near 22:00 LST have been chosen to demonstrate the procedure for data analysis. Because of the weighted average that was performed to reduce variations, only 10 sets of temporal profiles may be obtained from 16 sets of data.

Table IV. Two-Frequency Na Temperature Lidar Error Budget\*

Error Source	Parameter	Approximate Value	Temperature Error	Value at $T = 200$ K (K)
Laser frequency error	$\Delta\nu_a$	10 MHz	$0.25T (\Delta\nu_a/\sigma_D)^2$	0.02
	$\Delta\nu_c$	10 MHz	$0.15T (\Delta\nu_c/\sigma_D)$	0.7
Laser rms linewidth error	$\Delta\sigma_L$	0.5 MHz	$1.7T (\sigma_L/\sigma_D^2)\Delta\sigma_L$	0.06
Na radial velocity error	$V_R$	$< 3$ ms <sup>-1</sup>	$0.15T (V_R/\lambda_0\sigma_D)$	$< 0.34$
Na and atmospheric density variations	$\Delta\rho/\rho$	$< 1\%$ at 92 km	$0.5T (\Delta\rho/\rho)$	$< 1$
		$< 2\%$ at 92 + 5 km		$< 2$
		$< 5\%$ at 92 + 8 km		$< 5$
Photon noise	$N_s(z, \nu_a)$	$\sim 4000$ at 92 km	$0.8T/[N_s(z, \nu_a)]^{1/2}$	$\sim 2.5$
		$\sim 2500$ at 92 + 5 km		$\sim 3.2$
		$\sim 1400$ at 92 + 8 km		$\sim 4.3$

\* $T$  is the temperature (K);  $\sigma_D$  is the Na rms Doppler width = 456 MHz at 200 K;  $\sigma_L$  is the laser rms linewidth = 77.68 MHz;  $\lambda_0$  is the Na  $D_2$  wavelength = 589 nm;  $N_s(z, \nu_a)$  is the Na photon count at altitude  $z$  and laser frequency  $\nu_a$ .

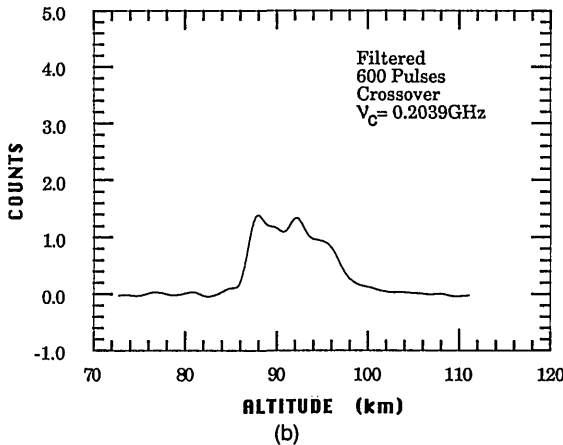
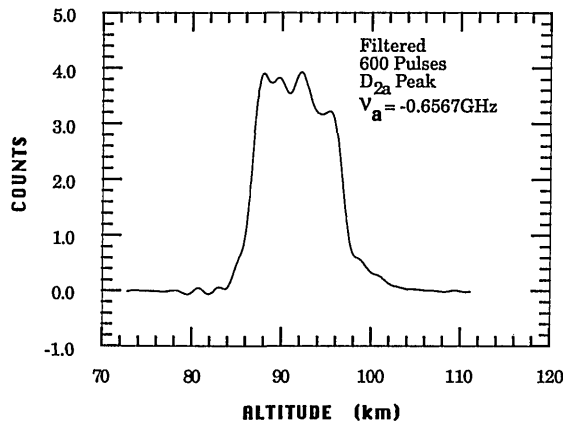


Fig. 11. Low-pass filtered profiles using the data that are shown in Fig. 10 at (a) the  $D_{2a}$  peak and (b) the crossover resonance.

After the background counts are subtracted, the profiles are each normalized to Rayleigh scattering at 30 km by using its own Rayleigh count averaged between 27.5- and 32.5-km altitudes. To carry out the normalization one must know the air density at 30-km altitude and the Rayleigh cross section of an air molecule. The air density at 30 km is taken to be  $3.83 \times 10^{17} \text{ cm}^{-3}$  from the table of the U.S. Standard Atmosphere<sup>24</sup> published in 1976. The short-term temporal air density variations<sup>25</sup> are at most  $\sim 1\%$  at a 30-km altitude; this is negligible after averaging over a 5-km interval. Seasonal variation of air density at a 30-km altitude does exist. Such a long-term variation, however, does not affect temperature determination by our ratio method. The Rayleigh cross section is taken to be  $\sigma_R = 3.46 \times 10^{-27} \text{ cm}^2$ , which is calculated for the Na  $D_2$  wavelength at  $\lambda_0 = 589.2 \text{ nm}$  from the measured values.<sup>26</sup> After background subtraction and Rayleigh normalization a representative set of profiles (at  $\nu_a$  and  $\nu_c$ ) from 73 to 111 km is shown in Fig. 10. To reduce the shot noise in the data each profile is Fourier transformed into its reciprocal (wave-number) space where a low-pass filter with a bandwidth depending on the desired spatial resolution is applied. For a 1-km resolution (corresponding to a filter cutoff of  $0.5 \text{ km}^{-1}$ ),<sup>27</sup> the filtered representative profile is inverse Fourier transformed back to its original

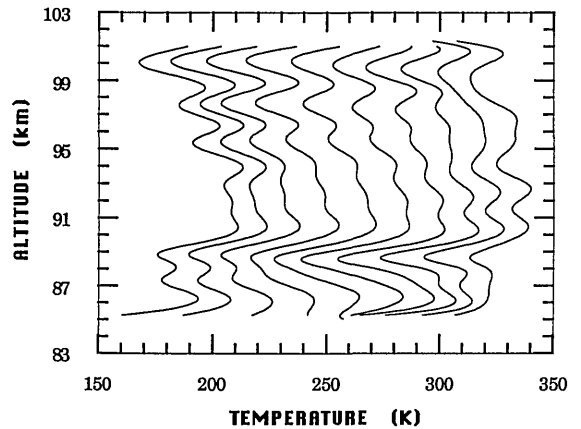


Fig. 12. Time series of temperature profiles at Fort Collins, Colo. ( $40.6^\circ\text{N}$ ,  $105^\circ\text{W}$ ), on 2 March 1990 from 20:00 to 22:10 LST. Each profile represents  $\sim 2.5$  min of data acquisition time with a profile separation of  $\sim 1$  min. The temperature scale applies to the first profile; successive profiles are spaced 15 K apart.

space, giving rise to the profiles that are shown in Fig. 11. The effect of low-pass filtering that reduces high-frequency noise is apparent. To minimize density variations the above discussed weighting factors are applied to the 16 profiles and 10 sets of photon-count profiles that are identified at the middle of the time intervals. The intensity ratio of the two profiles (the crossover to  $D_{2a}$ ) for each set yields a temperature profile (see Fig. 12). The temperature accuracy of the profiles that are shown in Fig. 12 was not analyzed in detail. It is expected, however, that, based on the values given in Table IV, a factor of 2 shorter in integration time (2.5 min) will reduce density variations by a factor of 2 and increase photon noise by a factor of 1.4, which gives rise to a temperature uncertainty of  $\pm 4 \text{ K}$  at the Na layer peak.

After the temperature profile at each temporal interval is determined a process of extinction compensation<sup>27</sup> is applied to determine the Na density profile from the corresponding photon-count profile. Because of the high spectral resolution that is used for the Na temperature lidar, the fluorescence cross

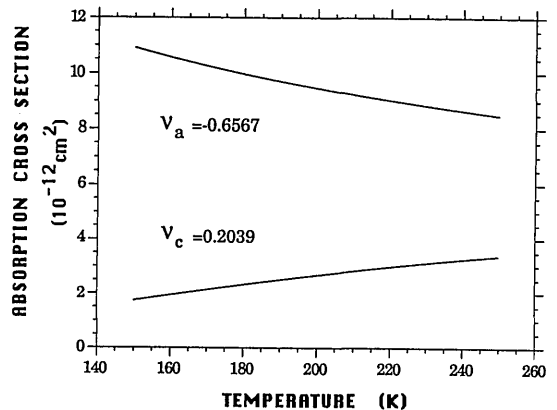


Fig. 13. Absorption cross sections at the  $D_{2a}$  peak ( $\nu_a = -0.6567 \text{ GHz}$ ) and the crossover resonance ( $\nu_c = 0.2039 \text{ GHz}$ ).

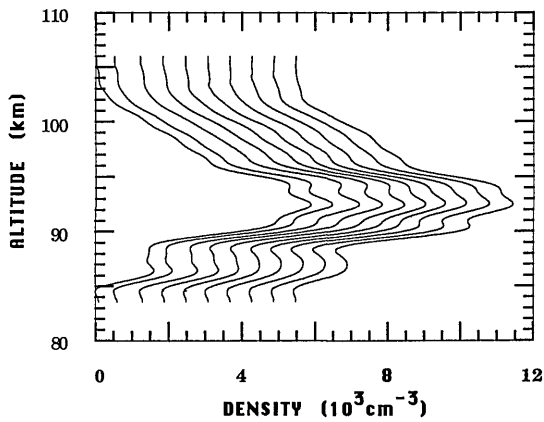


Fig. 14. Time series of density profiles deduced from the same data that are used for the temperature profiles shown in Fig. 12. The density scale applies to the first profile; successive profiles are spaced  $500 \text{ cm}^{-3}$  apart.

section is not only a function of wavelength but also a function of temperature. The temperature-dependent absorption cross section between the upper level 2 and the lower level 1 is

$$\sigma^A(\nu) = (g_2/g_1) (\lambda_0^2/8\pi) A_{21} g(\nu), \quad (3)$$

where  $(g_2/g_1)$ ,  $A_{21}$ , and  $g(\nu)$  are, respectively, the degeneracy ratio, the Einstein A coefficient, and the Doppler-broadened line-shape function given in Eq. (1). For the Na  $D_2$  transition  $(g_2/g_1) = 2$  and  $A_{21} = 6.289 \times 10^7 \text{ s}^{-1}$ . The fluorescence cross section at the  $D_{2a}$  peak ( $\nu_a = -656.7 \text{ MHz}$ ) and crossover ( $\nu_c = 203.9 \text{ MHz}$ ) may be deduced from the convolution of the laser line-shape function and the absorption cross section  $\sigma^A(\nu)$ . The results for the measured laser line-shape function given in Fig. 7(a) are shown in Fig. 13. Because the laser linewidth is much narrower than the Doppler width, fluorescence cross sections for different laser line shapes are nearly the same. By using these fluorescence cross sections, two density profiles may be obtained at each temporal interval after individual extinction compensation. The two density profiles at  $\nu_a$  and  $\nu_c$  are essentially the same because the same weighting factors are used to minimize the density variations. The Na density (which is averaged over the profiles at  $\nu_a$  and  $\nu_c$ ) at the 10 temporal intervals is shown in Fig. 14. Wave features are evident in both temperature and density profiles, Figs. 12 and 14, although their phase and amplitude are different. The geophysical implications of the data that were obtained in late summer 1989 and in late spring 1990 are being investigated and will be published elsewhere.

#### Summary and Future Extension of the Technique

The advances in laser technology in the past decade have made the concept of using the high-spectral-resolution Na  $D_2$  fluorescence for mesospheric temperature measurements a practical reality. The developments of Fricke and von Zahn,<sup>12</sup> and more recently of

She *et al.*,<sup>15</sup> have demonstrated beyond doubt the feasibility of routine high-resolution Na temperature measurements in the mesopause.

With the present lidar system,  $P_L A_R = 0.7 \text{ W m}^2$ , where  $P_L$  is the average laser power and  $A_R$  is the receiver aperture area, the photon noise and density variations dominate the temperature errors for short-term temperature measurements with an effective integration time of a few minutes. The temperature error resulting from the  $\pm 10\text{-MHz}$  laser-frequency uncertainty is negligible. However, for a lidar system with a larger  $P_L A_R$  product or for a temperature profile with a much longer time average, the error that results from photon noise and density variations near the Na peak may be much less than 1 K, in which case, the uncertainty in the position of the  $D_{2a}$  peak and crossover resonance and in the laser polarization relative to the Earth's magnetic field (the Hanle effect)<sup>28</sup> could become important. These systematic effects, however, can be corrected for with further study.

Because the laser frequency can in principle be controlled to submegahertz accuracy, it should be possible to measure horizontal wind velocities by measuring the associated Doppler shifts. Two sets of intensity ratios can be measured,<sup>19</sup> for example, one at the crossover and the  $D_{2a}$  peak and the other at an  $\sim 450\text{-MHz}$  shift to either side of the  $D_{2a}$  peak. With the lidar axis tilted  $20^\circ$  from zenith these ratios can be used to determine both temperature and horizontal wind speed. An alternative method is to measure the fluorescence returns at three different frequencies by locking the laser at the  $D_{2a}$  peak and sequentially shifting its frequency 443 and 886 MHz higher, for example, by the use of cascade or double-path acousto-optic modulators. This way the laser can be set sequentially at  $\nu_a$  ( $D_{2a}$  peak),  $\nu_a + 443 \text{ MHz}$ , and  $\nu_a + 886 \text{ MHz}$  on a shot-to-shot basis. Such a scheme would step rapidly to minimize the problem of density variation. Presumably the Na density does not vary significantly by a time scale of 0.1 s.

In short the feasibility of using high-spectral-resolution Na fluorescence lidar with the aid of Doppler-free saturated fluorescence spectroscopy for measuring mesospheric temperature profiles, which provide useful geophysical information, has been demonstrated. Its accuracy can be improved further, and with the availability of appropriate stable, tunable laser systems the technique can be extended to the probing of other atomic species, such as Fe and Ca, in the upper atmosphere. A simple modification of the two-frequency technique could lead to a simultaneous determination of density, temperature, and horizontal wind profiles.

The work of the Colorado State University group was supported in part by National Science Foundation grant ATM 88-20452 and carried out with equipment at the U.S. Army Research Office/Geoscience Center. The work of the University of Illinois group was supported in part by National Science Foundation grant ATM 88-11771.

## References

1. C. R. Philbrick, K. U. Grossmann, G. Lange, D. Offermann, K. D. Baker, D. Krankowsky, and U. von Zahn, "Density and temperature structure over northern Europe," *J. Atmos. Terr. Phys.* **47**, 159–172 (1985).
2. J. S. Theon, W. Nordberg, and L. B. Katchen, "The mean observed structure and circulation of the stratosphere and mesosphere," NASA Tech. Rep. TR-375 (1972).
3. G. G. Sivjee and R. M. Harnway, "Temperature and chemistry of the polar mesopause OH," *J. Geophys. Res.* **92**, 4663–4672 (1987).
4. D. G. Andrews, J. R. Holton, and C. B. Leovy, *Middle Atmosphere Dynamics* (Academic, San Diego, Calif., 1987).
5. M. L. Chanin and A. Hauchecorne, "Lidar observation of gravity and tidal waves in the stratosphere and mesosphere," *J. Geophys. Res.* **86**, 9715–9721 (1981).
6. C. Y. She, "Remote measurement of atmospheric parameters: new applications of physics with lasers," *Contemp. Phys.* **31**, 247–260 (1990).
7. H. Shimizu, S. A. Lee, and C. Y. She, "High spectral resolution lidar system with atomic blocking filters for measuring atmospheric parameters," *Appl. Opt.* **22**, 1373–1381 (1983).
8. C. S. Gardner, "Sodium resonance fluorescence lidar applications in atmospheric science and astronomy," *Proc. IEEE* **77**, 408–418 (1989).
9. G. Megie and J. E. Blamont, "Laser sounding of atmospheric sodium—interpretation in terms of global atmospheric parameters," *Planet. Space Sci.* **25**, 1093–1109 (1977).
10. E. Arimondo, M. Inguscio, and P. Violino, "Experimental determinations of the hyperfine structure in the alkali atoms," *Rev. Mod. Phys.* **49**, 31–75 (1977).
11. A. Gibson, L. Thomas, and S. Bhattachacharyya, "Laser observation of ground-state hyperfine structure of sodium and of temperatures in the upper atmosphere," *Nature (London)* **281**, 131–132 (1979).
12. K. H. Fricke and U. von Zahn, "Mesopause temperature derived from probing the hyperfine structure of the  $D_2$  resonance line of sodium by lidar," *J. Atmos. Terr. Phys.* **47**, 499–512 (1985).
13. U. von Zahn, K. H. Fricke, R. Gerndt, and T. Blix, "Mesospheric temperature and the OH layer height as derived from ground-based lidar and OH\* spectroscopy," *J. Atmos. Terr. Phys.* **49**, 863–869 (1987).
14. R. Neuber, P. von der Gathen, and U. von Zahn, "Altitude and temperature of the mesopause at 69° N latitude in winter," *J. Geophys. Res.* **93**, 11,093–11,101 (1988).
15. C. Y. She, H. Latifi, J. R. Yu, R. J. Alvarez II, R. E. Bills, and C. S. Gardner, "Two-frequency lidar technique for mesospheric Na temperature measurements," *Geophys. Res. Lett.* **17**, 929–932 (1990).
16. A. T. Ramsey and L. W. Anderson, "Pressure shifts in the  $^{23}\text{Na}$  hyperfine frequency," *J. Chem. Phys.* **43**, 191–194 (1965).
17. M. A. Kasevich, E. Riis, S. Chu, and R. G. Devoe, "rf spectroscopy in an atomic fountain," *Phys. Rev. Lett.* **63**, 612–615 (1989).
18. T. W. Hansch, I. S. Shahin, and A. L. Schawlow, "High-resolution saturation spectroscopy of the sodium D lines with a pulsed tunable dye laser," *Phys. Rev. Lett.* **27**, 707–710 (1971).
19. R. E. Bills, C. S. Gardner, and C. Y. She, "Narrowband lidar technique for sodium temperature and Doppler wind observations of the upper atmosphere," *Opt. Eng.* **30**, 13–21 (1991).
20. R. E. Bills and C. S. Gardner, "An advanced lidar data acquisition system," Tech. Rep. 88-001 (University of Illinois, Urbana, Ill., 1988).
21. G. Megie, F. Bos, J. E. Blamont, and M. L. Chanin, "Simultaneous nighttime lidar measurements of atmospheric sodium and potassium," *Planet. Space Sci.* **26**, 27–35 (1977).
22. B. M. Welsh and C. S. Gardner, "Nonlinear resonant absorption effects on the design of resonance fluorescence lidars and laser guide stars," *Appl. Opt.* **28**, 4141–4153 (1989).
23. J. R. Yu, H. Latifi, C. Y. She, J. H. Yee, and R. J. Niciejewski, "Simultaneous lidar and airglow temperature measurements in the mesopause region," *Geophys. Res. Lett.* **18**, 1361–1363 (1991).
24. *U.S. Standard Atmosphere*, NOAA-S/T76-1562 (U.S. Government Printing Office, Washington, D.C., 1976), p. 87.
25. C. S. Gardner, M. S. Miller, and C. H. Liu, "Rayleigh lidar observations of gravity wave activity in the upper stratosphere at Urbana, Illinois," *J. Atmos. Sci.* **46**, 1838–1854 (1989).
26. H. Inaba, "Detection of atoms and molecules by Raman scattering and resonance fluorescence," in *Laser Monitoring of the Atmosphere*, E. D. Hinkley, ed. (Springer-Verlag, New York, 1976), pp. 153–236.
27. C. S. Gardner, D. C. Senft, T. J. Beatty, R. E. Bills, and C. A. Hostetler, "Rayleigh and sodium lidar techniques for measuring middle atmosphere density, temperature and wind perturbations and their spectra," in *World Inosphere/Thermosphere Study Handbook*, C. H. Liu and B. Edwards, eds. (International Congress of Scientific Unions, Urbana, Ill., 1989), Vol. 2, pp. 148–187.
28. A. Corney, *Atomic and Laser Spectroscopy* (Clarendon, Oxford, 1977), Chap. 15, p. 473.